UC Berkeley
UC Berkeley Previously Published Works

Title

Cation valency in water-in-salt electrolytes alters the short- and long-range structure of the electrical double layer.

Permalink

https://escholarship.org/uc/item/3f11p61k

Journal

Proceedings of the National Academy of Sciences, 121(31)

Authors

Berlinger, Sarah

Küpers, Verena

Dudenas, Peter

et al.

Publication Date

2024-07-30

DOI

10.1073/pnas.2404669121

Peer reviewed

Cation valency in water-in-salt electrolytes alters the short- and long-range structure of the electrical double layer

Sarah A. Berlinger[a,1] ⓘ, Verena Küpers[b], Peter J. Dudenas[c] ⓘ, Devin Schinski[a], Lucas Flagg[c], Zachary D. Lamberty[a] ⓘ, Bryan D. McCloskey[a,d], Martin Winter[b,e], and Joelle Frechette[a,d,2] ⓘ

Affiliations are included on p. 8.

Highly concentrated aqueous electrolytes (termed water-in-salt electrolytes, WiSEs) at solid-liquid interfaces are ubiquitous in myriad applications including biological signaling, electrosynthesis, and energy storage. This interface, known as the electrical double layer (EDL), has a different structure in WiSEs than in dilute electrolytes. Here, we investigate how divalent salts [zinc bis(trifluoromethylsulfonyl)imide, $Zn(TFSI)_2$], as well as mixtures of mono- and divalent salts [lithium bis(trifluoromethylsulfonyl) imide (LiTFSI) mixed with $Zn(TFSI)_2$], affect the short- and long-range structure of the EDL under confinement using a multimodal combination of scattering, spectroscopy, and surface forces measurements. Raman spectroscopy of bulk electrolytes suggests that the cation is closely associated with the anion regardless of valency. Wide-angle X-ray scattering reveals that all bulk electrolytes form ion clusters; however, the clusters are suppressed with increasing concentration of the divalent ion. To probe the EDL under confinement, we use a Surface Forces Apparatus and demonstrate that the thickness of the adsorbed layer of ions at the interface grows with increasing divalent ion concentration. Multiple interfacial layers form following this adlayer; their thicknesses appear dependent on anion size, rather than cation. Importantly, all electrolytes exhibit very long electrostatic decay lengths that are insensitive to valency. It is likely that in the WiSE regime, electrostatic screening is mediated by the formation of ion clusters rather than individual well-solvated ions. This work contributes to understanding the structure and charge-neutralization mechanism in this class of electrolytes and the interfacial behavior of mixed-electrolyte systems encountered in electrochemistry and biology.

electrolytes | electrical double layer | solid-liquid interfaces | surface forces | scattering

Concentrated aqueous electrolytes (water-in-salt electrolytes, WiSEs) are omnipresent in biology and electrochemical systems, including in biological signaling, electrosynthesis, brine remediation/desalination, and aqueous batteries. Of particular note, WiSEs are gaining increasing attention because they display much wider electrochemical stability windows (>3 V) than the thermodynamic limit of water (≈1.23 V), making them exciting candidates for a variety of electrochemical systems including aqueous lithium-ion batteries (1). The low water-to-cation ratio leads to limited free water and the formation of heterogeneous ion clusters and networks (2–4). This unique solution structure is hypothesized to affect the properties (e.g., reactivity, conductivity, or viscosity) of these electrolytes. However, both the structure, particularly at an interface, and how it controls these properties are poorly understood.

Importantly, it is the arrangement of ions directly at the electrode-electrolyte interface that likely mediate electrochemical reactivity (5, 6). This ion arrangement, termed the electrical double layer (EDL), consists of ions and solvent molecules that accumulate near the solid surface to maintain charge neutrality (7, 8). The thickness of the EDL is given by an electrostatic decay/screening length, classically called the Debye length for dilute electrolytes. For concentrated electrolytes, and specifically for WiSEs, the nature of the EDL is more complex. Classical EDL theories including the Gouy–Chapman–Stern (GCS) framework do not hold (9–13). Motivated by lithium-ion battery applications, most experimental, theoretical, and simulation work has focused on lithium-based WiSEs, predominantly using lithium bis(trifluoromethylsulfonyl)imide (LiTFSI) (11, 12, 14–18). These prior studies revealed that the EDL is composed of multiple interfacial layers of ordered ions (11, 12, 14, 19) closest to the solid surface, followed by decay lengths that are much larger than a Debye length calculated based on the GCS description (i.e., the EDL is underscreened). This phenomenon is known as anomalous underscreening (referred to here simply as underscreening). This leads to EDL thicknesses that are larger than expected (upward of 50 nm). Beyond lithium-based WiSEs, both the layering structure

Significance

Knowledge of how ions arrange at interfaces is critical to understand charge-transfer behavior. Dilute electrolytes are well studied. In contrast, ion arrangement in concentrated and confined electrolytes is poorly understood and is particularly relevant for biological and electrochemical systems, which often exist in confined high-salt environments. Guided by theory, we use a multitechnique analysis of independent experiments that allows us to infer insights into the structure of mono- and divalent electrolytes under confinement. We link bulk and interfacial structure and reveal that the charge-neutralization mechanism is likely mediated by ionic clusters, rather than bare (solvated) ions. These findings pave the way for innovative theory and understanding of interfacial behavior of multivalent and mixed-valency electrolytes, critical for many real-world electrolyte systems.

[1]Present address: Energy Conversion Group, Energy Storage and Distributed Resources Division, Lawrence Berkeley National Laboratory, Berkeley, CA 94720.

[2]To whom correspondence may be addressed. Email: jfrechette@berkeley.edu.

and underscreening have been observed in other concentrated electrolytes, including other WiSEs (11–14, 20–23) and ionic liquids (10, 24–31) (ILs) primarily via surface forces measurements, X-ray reflectivity, or fluorescence measurements. However, while underscreening is generally attributed to ion–ion correlations, the exact origin of these long electrostatic decay lengths is still actively debated (9, 10, 26, 32–45). Both the short-range layering structure (<10 nm from a solid-liquid interface) as well as longer-range charge-neutralization decay lengths (10 to 50 nm from a solid-liquid interface), are critical to understand interfacial reactivity.

In this work, we aim to understand how multivalent cations in WiSE electrolytes alter both the short-range and long-range signatures of the EDL, particularly under confinement. For most electrochemical and biological systems, reactions occur within a confined pore of a porous electrode or within a molecularly crowded biological environment. While there exists some theoretical work describing how divalent electrolytes alter the EDL (46), the experimental evidence is more scarce. Moreover, our understanding is even more limited for mixed valency ions or for confined (or overlapping) EDLs. While single-cation studies have certainly helped build our understanding of the EDL, many energy (47–52) and biological (53–57) applications use mixed-cation systems (including mixed-cation salts). Divalent ions can form multidentate bonds which we expect to alter the short-range structure at an interface. Additionally, electrostatic interactions (dipole, Coulomb, charge, etc.) all depend on valency. We therefore hypothesize that underscreening will be altered when comparing monovalent and divalent WiSEs. Furthermore, exploration of underscreening as a function of valency should provide insight into the mechanistic origins of these phenomena.

Here, we probe how divalent cations order at charged interfaces in concentrated aqueous environments, both as the only cation and in mixtures of other cations. We choose $Zn(TFSI)_2$ as the divalent salt due to its relevance for aqueous Zn–ion batteries (47, 58). In the first part of this paper, we establish the bulk structure of LiTFSI, $Zn(TFSI)_2$, and two mixtures of LiTFSI and $Zn(TFSI)_2$ WiSEs via wide-angle X-ray scattering (WAXS) and Raman spectroscopy. The data reveal that all electrolytes form clusters, as seen for pure LiTFSI WiSEs via molecular dynamics (MD) simulations (3, 59), and that the anions exist within the cation solvation shells. We then report on the EDL structure under confinement for the same series of WiSEs using a Surface Forces Apparatus (SFA), an instrument uniquely suited to characterize the EDL under confinement. The forces measured in the SFA can be converted to an interaction potential, a necessary dataset to verify double-layer theories and to quantify fluid layering away from a solid surface. Here, we study surface forces as a function of confinement to measure the adsorbed ion-layer thickness (adlayer), the layering structure at a solid-electrolyte interface, and the electrostatic decay length, to reveal that both the anion and cation play critical roles in all parts of the EDL. While the ionic species chosen are directly relevant for battery applications, the understanding gained here is translatable to any complex (and more general) multi-ion application.

Results and Discussion

Bulk Electrolyte Characterization. We use four electrolytes with LiTFSI:$Zn(TFSI)_2$ molality (moles solute/kg water, m) ratios of 10:0, 10:1, 7:2, and 0:3 (i.e., 10:1 is 10 m LiTFSI mixed with 1 m $Zn(TFSI)_2$ dissolved in water). The ratios are chosen to slowly increase the concentration of $Zn(TFSI)_2$ while decreasing the concentration of LiTFSI, moving from pure LiTFSI to pure $Zn(TFSI)_2$, while being mindful of the much lower solubility limit of $Zn(TFSI)_2$ (60) compared with that of LiTFSI (~3.5 m $Zn(TFSI)_2$ vs. >21 m LiTFSI). For context, at these solubility limits for 3.5 m $Zn(TFSI)_2$ in water, there are roughly 16 water molecules per cation, while at 21 m LiTFSI, there are only 2.6 waters per cation (*SI Appendix*, Table S1). Therefore, lower LiTFSI concentration than the prototypical 21 m is chosen here to maintain a more similar water environment across the salt series. As a reference, in a dilute electrolyte, Li$^+$ will have roughly four water molecules in a primary solvation shell, while Zn^{2+} will have six (58). The electrolyte concentrations, their known materials properties, and quantities characterized in this work are shown in Table 1. Note that Table 1 summarizes values that are determined throughout the rest of this paper and will be referred to throughout. Additional details on the calculations in Table 1 are presented in the *SI Appendix*.

We begin our analysis by exploring the bulk TFSI$^-$ arrangement via WAXS. The WAXS data are shown in Fig. 1*A* in which the capillary background is subtracted (see *SI Appendix*, Fig. S1 for unsubtracted data and the empty capillary background). Distinct peaks are observed for each electrolyte. Our 10:0 and 10:1 data agree with previously reported LiTFSI and $Zn(TFSI)_2$ WiSEs (58, 59, 62–65). Therefore, we use these previous works to interpret our WAXS data. MD simulations show that there are two characteristic WAXS peaks that are due to different TFSI$^-$–TFSI$^-$ arrangements. The peak at around 0.5 Å^{-1} (larger real space, leftmost peak in Fig. 1*A*) corresponds to correlation distances between anions solvated by water and separated by additional water molecules, while the peak around 1 Å^{-1} (middle peak in Fig. 1*A*) is due to anion–anion spacing within an ionic cluster and/or network (i.e., the anions are closely associated with each other because their solvation shells contain a mixture of anions and water molecules, or because the anions are separated by only one water molecule in a TFSI–H_2O–TFSI cluster) (59, 62–65). An ionic network forms when multiple clusters come together, but we note that WAXS data cannot distinguish between clusters and networks because the spacing within a single cluster is the same as (or very similar to) spacing within many clusters joined together. Despite this, MD simulations of LiTFSI WiSEs suggest that these percolating anion networks form at concentrations greater than those considered here (2). Therefore, throughout we refer to this anion–anion structure

Table 1. Electrolyte properties for LiTFSI and Zn(TFSI)₂ WiSEs

LiTFSI (m)	Zn(TFSI)$_2$ (m)	Mass fraction	Density (51) (kg/m^3)	LiTFSI (mol/L)	Zn(TFSI)$_2$ (mol/L)	H$_2$O (mol/L)	ϵ(18)	a(nm)	λ_D(nm)	$\frac{\lambda_F}{\lambda_D}$	$\frac{a}{\lambda_D}$
10	0	0.74	1,581	4.08	0.00	22.69	19.8	0.642	0.076	207	8.45
10	1	0.78	1,628	3.62	0.36	20.12	15.9	0.625	0.064	280	9.77
7	2	0.77	1,611	2.65	0.76	21.01	17.1	0.605	0.064	356	9.45
0	3	0.65	1,480	0.00	1.54	28.58	31.9	0.613	0.090	144	6.81

a is taken from the WAXS cluster d-spacing in Fig. 1*C*. The last two columns are the data plotted in Fig. 6*B*.
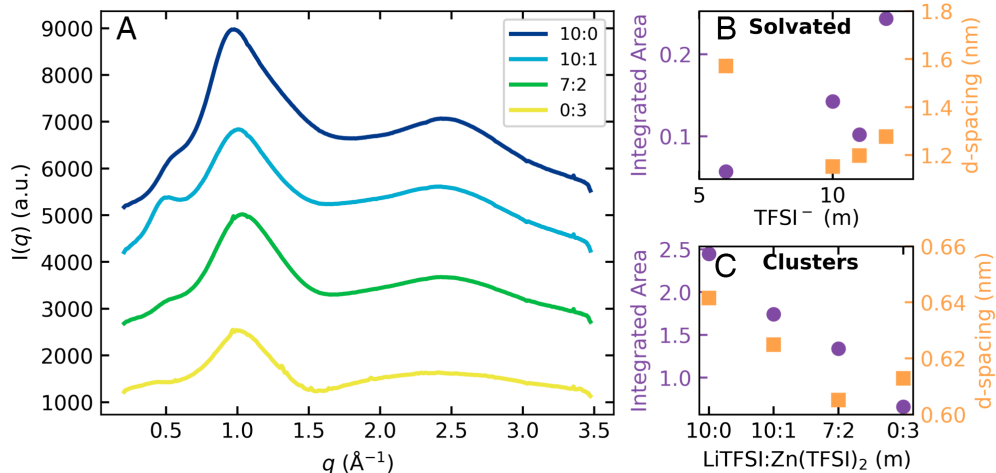
Fig. 1. Transmission WAXS experiments of bulk electrolytes. (*A*) Background-subtracted linecuts showing the intensity (*I(q)*, a.u.) as a function of the scattering vector, *q*. Labels describe the ratio of LiTFSI to Zn(TFSI)$_2$ in molality (e.g., 10:0 is 10 m LiTFSI, 0 m Zn(TFSI)$_2$), see Table 1. Extracted integrated area (purple circles) and real-space d-spacing (orange squares) for (*B*) the solvated anion peak (≈0.5 Å^{-1} in *A*) and (*C*) the anion cluster peak (≈1 Å^{-1} in *A*). Note that the *x* axis scaling is different in (*B*) and (*C*).

peak at ≈1 Å^{-1} as spacing within a cluster. The shoulder in the cluster peak around 1.5 Å^{-1} corresponds to anions directly in contact with each other within the network (62, 63). Using the above interpretation of the data, we analyze each of the two TFSI$^-$–TFSI$^-$ peaks in Fig. 1 *B* and *C*. Fig. 1*B* shows the integrated area of the solvated anion peak (indicative of the degree of ordering) as well as the corresponding real-space domain (d-) spacing (spacing between solvated anions). In Fig. 1*C* we plot the anion-cluster peak, summing the peaks associated with the cluster/network structure (main peak and shoulder defined above) for the integrated area, representing anions within these ionic clusters. The right-most peak around 2.5 Å^{-1} scales with cation concentration and is likely related to cation solvation structures (either via water or TFSI$^-$) (64); however, additional simulations would be needed to determine the exact structures.

The solvated anion peak (0.5 Å^{-1}) is highly influenced by ionic strength. This is evident because the 10:1 electrolyte has the strongest ordering (largest integrated area in Fig. 1*B* and highest TFSI$^-$ concentration), likely because this electrolyte has the greatest concentration of TFSI$^-$ as compared with the other electrolytes (Table 1). For reference, TFSI$^-$ concentration increases according to 10:1 > 7:2 > 10:0 > 0:3. Additionally, the d-spacing for the 0:3 electrolyte is significantly larger than the other electrolytes and the 0:3 electrolyte has the greatest concentration of water.

Furthermore, addition of Zn^{2+} disrupts the ionic clusters. We see a very strong effect of Zn^{2+} concentration on cluster formation in Fig. 1*C*: as the divalent ion concentration increases, the peak area steadily decreases to less than 30% of its baseline value. This is likely because Zn^{2+} has a higher hydration number than Li$^+$: the stronger preference for water molecules surrounding the Zn^{2+} cation would reduce anion–anion proximity. Because the Zn^{2+} is less likely to desolvate, the presence of additional water molecules would disrupt anion–anion interactions, leading to reduced cluster formation. It should be noted that differences in the partial scattering functions of Li$^+$ and Zn^{2+} (due to differences in electron density) may also play a role in the decrease in peak area with Zn^{2+} concentration. Destructive interference from Zn^{2+} cation scattering could cause a decrease in the peak area, though we believe to be a minor effect; if the Zn^{2+} was highly structured such that destructive interference was the dominant cause in the decreased peak area, one would expect to see scattering from the Zn^{2+} structure elsewhere in the data. This is not observed, thus we believe this to be a minor effect.

To complement the anion–anion arrangement information gained from the WAXS data, we characterize the cation–anion solvation structure and water coordination environment via Fourier-transform (FT) Raman spectroscopy. The Raman band at wavenumber (*ν*) ≈ 742 cm^{-1} is associated with the expansion and contraction of TFSI$^-$ and can be used to assess the anion coordination environment. The maxima of this band as a function of salt concentration and the spectra between 720 ≤ *ν* ≤ 780 cm^{-1} for different TFSI$^-$-based electrolytes are plotted in Fig. 2 *A* and *B*. A shift toward higher
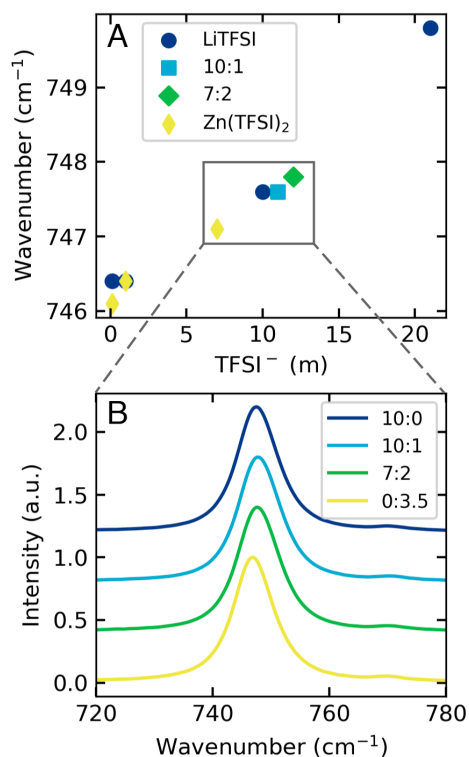

Fig. 2. Raman spectroscopy results of bulk LiTFSI and Zn(TFSI)$_2$ electrolytes. (*A*) Maxima of the Raman bands associated with TFSI$^-$ (720 ≤ *ν* ≤ 780 cm^{-1}) for pure LiTFSI and Zn(TFSI)$_2$ WiSEs as well as two mixed-salt electrolytes as a function of TFSI$^-$ concentration. (*B*) The normalized Raman spectra of the four electrolytes used in this study and shown in the boxed region in (*A*), displaying the TFSI$^-$ band (720 ≤ *ν* ≤ 780 cm^{-1}). Concentrations of LiTFSI:Zn(TFSI)$_2$ are in molality.

wavenumbers is associated with stronger coordination (66, 67), indicating interactions between the anion and the cation. The Raman shift of LiTFSI-based WiSEs increases with increasing salt concentration (1). This is observed here for both LiTFSI- and Zn(TFSI)$_2$-based electrolytes (Fig. 2*A* and *SI Appendix*, Fig. S7), suggesting stronger interactions between TFSI$^-$ and the cation with increasing concentration for both salts, as well as the formation of contact-ion pairs (CIPs, one anion per cation) and aggregates (Aggs, multiple anions per cation). No significant differences are obtained for the Raman spectra of 10:0, 10:1, and 7:2 (Fig. 2*B*); all demonstrate the formation of CIPs or Aggs, based on their Raman shift > 742 cm^{-1}. The 0:3.5 electrolyte has a slightly smaller Raman shift but scales with the trend for TFSI$^-$ concentration (Fig. 2*A*); the lower salt concentration likely accounts for this difference.

Prior MD simulations have reported conflicting Zn^{2+} solvation structures in similar mixed LiTFSI/Zn(TFSI)$_2$ WiSE systems: Zn(H$_2$O)$_6$ structures (58) as well as TFSI$^-$ within the Zn^{2+} solvation shells forming species such as Zn(TFSI)$_2$(H$_2$O)$_2$ (47). Our Raman results here support the latter for all electrolytes because they all exhibit cation–anion interactions. Additionally, deconvolution of the Raman band into CIPs, Aggs, and solvent-separated ion pairs (SSIPs) similarly shows no substantial differences between the electrolytes (*SI Appendix*, Fig. S8 and Table S1), suggesting similar levels of cation–anion interactions across the four electrolytes. However, quantitative interpretations of the deconvolution may not be appropriate because the three peaks are not distinct, see *SI Appendix*. Note that the SSIPs or CIPs/Aggs from the Raman spectroscopy should not be confused with the solvated anions or anion clusters from the WAXS data, because they measure different interactions (anion–cation vs. anion–anion, respectively). Additionally, the Raman shift of the O–H peak (*SI Appendix*, Fig. S9) suggests similar water environments across the four electrolytes.

Based on insights from both the WAXS and Raman data, we can infer potential bulk structures, shown schematically in Fig. 3. From our bulk data, all electrolytes have anion–cation interactions, with the anions likely in the cation solvation shells. The TFSI$^-$ exists both as free solvated ions and within a more condensed cluster. Because the cations are strongly associated with the anions, they likely have similar population distributions as the anions. Addition of Zn^{2+} does not seem to alter the cation-solvation structure but rather alters (suppresses) clustering of these cation–anion complexes.

EDL Under Confinement. Having gained an understanding of the bulk structure of each of our four electrolytes, we next focus on characterizing the EDL at a charged interface under
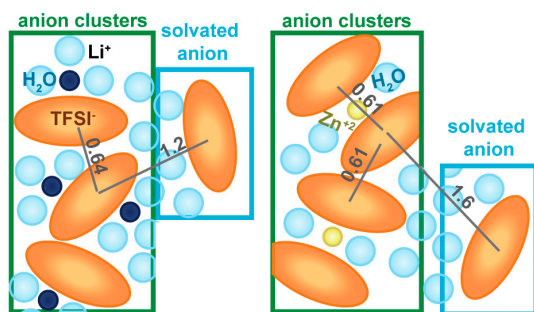

Fig. 4. Representative force curves normalized by the radius of curvature (F/R) as a function of separation distance between the two mica surfaces as they approach each other. Between the surfaces are WiSEs composed of LiTFSI:Zn(TFSI)$_2$ ratios (in molality) (*A*) 10:0, (*B*) 10:1, (*C*) 7:2, or (*D*) 0:3. *Insets* display the same data with extended *x*- and *y*-axes. Features such as layering transition (LT), compression (Comp), closest approach, and electrostatic decay length are labeled.

Fig. 3. Possible network and solvent-separated anion pair arrangement. Note that this may not be the exact structure but is drawn to scale taking into account the WAXS spacing we measure (Fig. 1), ionic radii (11), solvation shell structure, and g(r) from MD (47) simulations. Numbers denote lengths in nanometers.
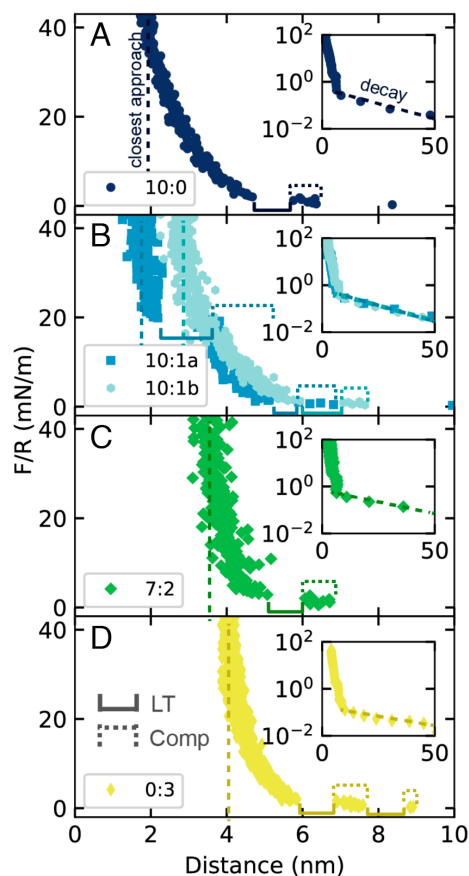
confinement. With an SFA, we use confinement as a tool to unravel both short-range and long-range interactions between opposing surfaces. Here, our solid-electrolyte interfaces are formed with mica. Mica is chosen as an inert, charged, atomically smooth model surface. In our experiments, we confine the electrolytes between two mica surfaces and measure the forces between them on successive approach and retraction curves. These forces are a direct manifestation of the interaction potential between the surfaces. Additional details on the SFA measurement technique are discussed in Supporting Information and reviewed in refs. 7, 68, and 69. In dilute electrolytes, mica has a negative surface potential ($\approx$–100 mV relative to the bulk electrolyte), in which the exact value depends on the nature of the electrolyte and its concentration (70–74). One would therefore expect the cation to be the predominant ion within the EDL. However, we note that charge reversal of mica has been previously observed in the presence of a divalent electrolyte (75), as well as for silicon oxide surface in contact with monovalent electrolytes at very high concentrations (13). Despite not knowing the sign of surface potential, as will be revealed below, both the cation and the anion seem to play integral roles throughout the whole EDL.

Representative approach force curves are shown in Fig. 4 *A*–*D* for each salt, displaying the normal force normalized by the radius of curvature of the mica surfaces at a given surface separation. This normalization allows for quantitative comparison across different

experiments and surface geometries according to the Derjaguin approximation, $\frac{F(D)}{R} = 2\pi W(D)_{flat}$, where $W(D)_{flat}$ is the interaction energy between two flat surfaces separated by a distance, D (7). The surfaces begin initially at $4\approx 00$ nm apart, at which point the force is zero. For each salt, the first force that is felt as the surfaces are brought closer is an exponentially increasing repulsive force. In classical EDL theories, the slope of this exponential force is the Debye length. Here, we assume this force is also an electrostatic decay length, in agreement with previous works on concentrated electrolytes and ionic liquids (10, 11); however, we note that this measured decay length does not correspond to the Debye length, as will be discussed below. As the mica surfaces move closer, the next feature we see are discontinuities in the force curve, beginning at ≈ 10 nm. These discontinuities are indicative of oscillatory (hydration) forces caused by the layering of hydrated ions and are called ordered layering transitions (LTs) or film-thickness transitions (76, 77). Physically, if a layered fluid is confined between two flat plates and then squeezed, the force required to squeeze the layer of hydrated ions would initially increase as that layer is compressed and the ions within that layer order and resist further confinement ("compression"). Above a certain force, that layer will be expelled into the surrounding reservoir, exhibiting a LT, and the surfaces will "jump" closer into contact. These compressions and LTs provide the length scale of molecular ordering in the fluid. We note that for the 10:1 data, in about half of our experiments, we saw a second LT and have labeled these data 10:1a, versus the data with only one LT, 10:1b. The two types of 10:1 data overlap until that second LT. The force is lower in 10:1a; it is possible if we applied additional force, we would see that second LT in the 10:1b data as well. For most of the analysis, we combine these two data types, but for the sake of transparency when analyzing the LT, we leave them distinct (see SI for more details). Additionally, our criteria for identifying LTs were strict: the size of the discontinuity must be larger than the error in our x-axis resolution (typically around 1 to 2 Å), be larger than the distance between the previous two points, and the LT must be reproducible (appearing in multiple approach curves). We therefore note that there could be small LTs on the order of a few angstroms that we omit. The last feature in the approach curve is the final position of the surfaces, termed the closest approach. Any deviation from a separation of zero thickness suggests that the surfaces are not in contact, but instead, something is strongly adsorbed to their surfaces. The adlayer thickness on each surface is the closest approach divided by two, assuming a symmetrical system. Representative retraction data, displaying dynamic behavior indicative of ion reorganization, is shown in *SI Appendix,* Figs. S12–S15.

Groves et al. (11). and Han et al. (12) have previously measured surface forces in 11.64 m and 10 m LiTFSI, respectively. While there are slight differences between all our studies, our data agree qualitatively and are in particularly good agreement with those of Han et al., thus confirming our methodology and reproducing their findings. The Groves et al. study achieved a better force resolution than either we or Han et al. did, allowing them to resolve additional LTs. While it is possible there may be additional LTs that we omit due to our strict criteria defined above, our study is clearly able to resolve the more tightly bound reproducible layers closest to the interface, which are the most relevant layers for electrochemical applications, and does so in a consistent manner across all electrolytes, allowing for quantitative comparison. We begin our analysis with the closest approach and work our way outward within the EDL.

A higher concentration of $Zn(TFSI)_2$ contributes to a thicker adlayer. As seen in Fig. 5A, the closest approach data range from an average value of ≈ 2 nm to 4.5 nm, shifting steadily outward as the
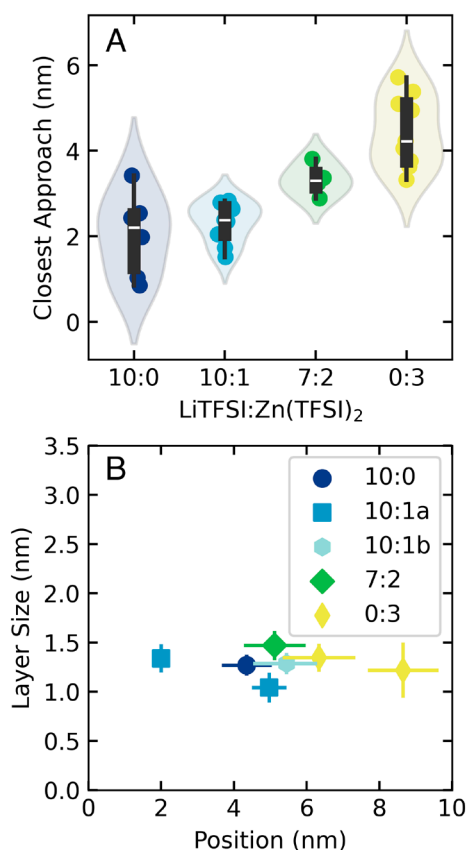

Fig. 5. Features extracted from force curves, as defined in Fig. 4, including (*A*) the closest approach position in which labels denote molality. (*B*) Layer size plotted as a function of where the LT occurs (LT end, leftmost point of LT) for each electrolyte.

$Zn(TFSI)_2$ concentration increases (with the exception of the 10:1a that was able to achieve an additional LT). This indicates the adlayer thickness on each mica surface grows from ≈ 1 nm to 2.25 nm, independent of ionic strength. In this closest-approach region, increasing Zn^{2+} concentration also yields higher forces at the same separation distance, indicative of larger oscillatory hydration forces in the $Zn(TFSI)_2$ case, as has previously been seen for divalent ions (21). The values of the adlayer thicknesses are too large to be bare cations (≈ 0.5 nm). It is therefore likely that the adlayer includes hydrated cations and that these cations also contain $TFSI^-$ anions in their solvation shells (as they do in the bulk), given their nm-scale sizes (the end-to-end length of $TFSI^-$ is around 1 nm (11)). We note that the SFA cannot distinguish chemical identity, and so we cannot determine the species identity at the surface. However, previous work has suggested that the competitive adsorption between monovalent and divalent ions on a mica surface is driven not by valency but rather by hydration forces: It is less favorable for more strongly hydrated ions (such as the Zn^{2+}) to adsorb to a surface than weakly hydrated ions (as compared with Li^+) (78). Similar conclusions have been drawn about IL-salt mixtures on graphene walls: Less-hydrated monovalent ions exist in greater abundance near the interface than do the more-hydrated divalent ions, which retain similar solvation shells as in the bulk (79). The weaker hydration of Li^+ could explain why we do not see a step change to a larger adlayer thicknesses once a small amount of Zn^{2+} is added, which would be the case if we had preferential adsorption of Zn^{2+} over Li^+ (Zn^{2+} has a larger solvation shell). The adlayer is a complex network of cations, anions, and water molecules and its thickness continues to increase with the concentration of Zn^{2+} in solution.

All electrolytes display a distinct layering structure at the mica-electrolyte interface. This is seen in Fig. 5B, in which we plot the LT length as a function of where the LT occurs for each electrolyte. Interestingly, a small amount of the divalent ion as shown in 10:1a seems to induce a small amount of ordering: two LTs are observed for 10:1a and also the pure 0:3 Zn²⁺ case, while only one LT is observed for the remaining electrolytes. It is possible the divalent ion induces more order at the interface due to multidentate binding. Notably, within error all the LTs are the same size across the electrolytes. This suggests that the layer size is governed by what is similar between them (the anion) and not what is different (the cation). Interestingly, the LT size is also similar to the solvated TFSI⁻ peak spacing in the WAXS data (Fig. 1B), around 1.3 nm, further supporting the idea that layer spacing is controlled by the anion. Similar anion-size-controlled structures have also been observed in bulk WiSEs (80). Solvated anion accumulation at the interface is also consistent with the hydrophilic nature of the mica surface. The corresponding compressions prior to each LT are shown in *SI Appendix*, *Fig. S11*. Again, all compressions have a similar size (around 0.5 nm) with the exception of the much larger compression size in the 10:1a electrolyte, suggesting perhaps a looser structure of the ordered layers for this electrolyte due to the mixture of ions.

The final feature is the long-range electrostatic decay length. In classical Debye–Hückel theory, the decay length is termed the Debye length and is the characteristic length scale obtained from the Poisson–Boltzmann equation:

$$\lambda_D = \kappa_D^{-1} = \left(\frac{\epsilon \epsilon_0 k_b T}{e^2 \sum_i \rho_i z_i^2} \right)^{\frac{1}{2}}, \qquad [1]$$

in which ϵ is the vacuum permittivity constant, ϵ_0 is the dielectric constant of the media (which is a strong function of salt concentration), k_b is the Boltzmann constant, T is temperature, e is the elementary charge, and ρ_i is the number density and z_i is the charge (valence) for an ion species i. The Poisson–Boltzmann equation treats ions as point charges and does not consider any ion–ion correlations. For context, the calculated λ_D for our four electrolytes are on the order of 1 Å (Table 1).

In Fig. 6A, we plot the measured decay lengths from our SFA experiments, obtained by fitting $e^{-\kappa_F D}$ to our long-range force data in the decay region labeled in Fig. 4. Here, we use the subscript F to denote that it was fitted from our data, rather than the calculated Debye length from classical theory. We note that we can precisely determine the decay length for a given approach curve. While we do not have a lot of points in our fit region due to the motor step size, the data cover around a decade, and the fit is weighted by our force resolution which is typically ≈ 0.02 mN/m. On average, fit values have SD < 2 nm. Because the spread in our data is significantly larger than the error associated with calculating each decay length, we conclude that there is substantial variability in the magnitude of the decay length across different approach curves. The random nature of the decay length in WiSEs has also been reported by Han et al. (12) For comparison, imidazolium ILs display gradual changes in the measured decay length value over the course of many hours (24). We did not observe any similar systematic changes over time for these electrolytes during our experiments, which we monitored typically for ≈ 30 h. Therefore, it is not immediately evident why these WiSEs exhibit these stochastic decay lengths but is likely due to the formation and disruption of ionic clusters, as discussed below.

Notably, when analyzing the magnitude of the decay lengths, there does not seem to be great variability between all four salts. This is initially surprising because one expects the decay length, which is electrostatic in origin, to be strongly influenced by valency. Within error, we see no change between the 10:0, 10:1, and 7:2 electrolytes, suggesting that the decay length is not mediated solely by the bare cation (or anion). We note that while the 0:3 electrolyte does have a slightly smaller decay length, it also has the lowest ionic strength; decoupling decay length, valency, and ionic strength are not obvious within this concentrated environment.

Our measured λ_F values are over two orders of magnitude larger than λ_D. For reference, λ_D values on the order of ≈ 10 nm are achieved when salt concentrations approach less than 1 mM, or $\approx 0.03\%$ of our salt concentrations, suggesting we are clearly in the underscreening regime. Gebbie et al. originally attributed underscreening to a lack of ion dissociation (25) if a large number of ions exist as neutral ion pairs, the effective ion concentration would be dramatically lower than the real value. Along similar ideas, Kjellendar proposed to replace the static dielectric constant with an effective dielectric permittivity, arguing that the static dielectric constant is not applicable in these dense salt environments (39, 40). By also replacing the ion charge with an effective charge, they arrive at an identical expression as the Debye–Hückel
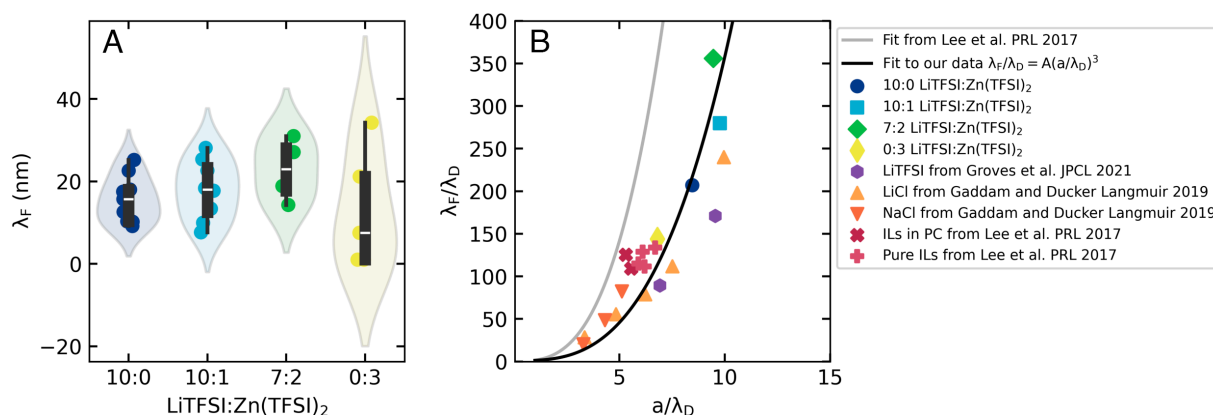

Fig. 6. Decay length scaling analysis. (*A*) The measured decay length, λ_F, for all electrolyte concentrations, in which labels denote molality. (*B*) Ratio of λ_F, over the Debye length, λ_D, plotted vs. the average ion diameter, a, also scaled by the λ_D. Fit lines are from the Lee et al. (9) scaling analysis and from fitting that cubic relationship to our four electrolytes. Superimposed are data points of other concentrated electrolytes from refs. 9, 11, 13. For our data, a is taken as the cluster spacing from the WAXS measurements in Fig. 1*C*.

expression but with renormalized terms. Lee et al. conducted a scaling analysis (9), and found that

$$\frac{\lambda_F}{\lambda_D} \sim \left(\frac{a}{\lambda_D}\right)^3,$$ [2]

or,

$$\lambda_F \sim \lambda_B a^3 c_{ion},$$ [3]

in which a is the average ion diameter, c_{ion} is the ion concentration, and λ_B is the Bjerrum length, defined as

$$\lambda_B = \frac{z^2 e^2}{4\pi\epsilon\epsilon_0 k_B T}.$$ [4]

This scaling analysis was motivated by the picture of a neutral salt lattice, in which screening occurs via defects in the lattice (i.e., water molecules). We note that scaling by λ_D is not a natural choice for high-concentration electrolytes and does not make much physical sense when it becomes smaller than a. However, it is used to amplify the deviation from classical theory.

In our experiments, we directly measure λ_F/λ_D. However, the value to choose for a is not immediately obvious because the cation and anion are very differently sized and are both within each other's solvation shells. In Fig. 6B, we plot the Lee et al. scaling analysis, reproducing their original fit line (gray line) (9). If we look at the intersection of our λ_F/λ_D values with fit line from ref.9, the recovered ion diameter is between 0.4 nm and 0.45 nm for all salts. This is unexpected because the solvated Zn^{2+} complex is larger than that of Li^+. If the definition of a is truly the average ion diameter, we would 1) expect a to change across the different electrolytes more than it does here and 2) be larger, given the dimensions and spacings of all ions. Likely, we lie off the line to the right. Other groups have similarly noted that not all data fall on this line (13, 27, 31). In fact, in the original scaling analysis, pure ILs and the highest concentrations of IL in solvent also lie off the line to the right (9). Additionally, they noted previously that depending on the definition of a, multiple scaling lines may be recovered (26).

Recently, Brownian Dynamics (42) and the Restricted Primitive Model (32) have reproduced the underscreening phenomena by introducing ionic clusters to the models, motivating additional cluster-based scaling analysis (81). While the cluster size is treated as an adjustable parameter, the concept of ion clusters makes sense, especially in the context of WiSEs, given that $TFSI^-$ is in the cation solvation shells and the ions form clusters as shown in our data. Furthermore, MD simulations demonstrate that ionic aggregates and ion networks/gels in ILs can influence ionic screening (82, 83). Additionally, Härtel et al. (32) found that while λ_F/λ_D does scale according to a/λ_D, the exact curve is not universal, in agreement with our observations and those of others discussed above. They conclude that the data by Lee et al. appear to have a universal trend because all data coincidentally fall on the same curve when comparing reduced temperature and reduced concentration values. Consistent with our hypothesis that we lie to the right of the Lee et al. fit, our data lie on a separate curve in the reduced parameter space (*SI Appendix*, Fig. S10).

Within our experiments, we have independent measurements of both the y- and x-axes in this scaling-law plot. Motivated by this cluster idea, we set a in Fig. 6B for each of our electrolytes as the cluster spacing from the WAXS data (black line). We then fit this cubic scaling law to our data and recover an excellent fit that is indeed to the right of the original fit line. This is encouraging and suggests that the long-range decay is mediated by ion clusters. We also superimpose data of other systems, including the higher-concentration IL data that deviated from the fit in ref. 9,

LiTFSI WiSE data from ref. 11 using the same WAXS spacing for our LiTFSI data, and highly concentrated LiCl and NaCl in water solutions from ref. 13 using the salt lattice parameter (84) for a (*SI Appendix*, Tables S2–S4). All these systems should be governed by similar physics, particularly because ϵ is very low in these concentrated-salt environments; the lack of bulk water and low permittivity could render water and organic solvent systems similar. Indeed, the above data agree well with our fit line and demonstrate that in these highly concentrated mixtures, solvent may act to swell the clusters and shift the curve to the right.

These ion clusters help explain both the decay length's insensitivity to valency and its seemingly random behavior. From our WAXS data, we observe that the anion clusters are suppressed as Zn^{2+} concentration increases (Fig. 1). λ_F may therefore remain similar with increasing valency because the charge-neutralization mechanism (via anion–anion cluster formation) is disrupted as the divalent ion concentration increases, likely due to higher hydration number of Zn^{2+} versus Li^+. Additionally, Härtel et al. (32) reveal that the y-axis value in Fig. 6B can shift significantly depending on the size of the ionic cluster, and perhaps that helps explain the spread in our measured λ_F values: due to the dynamic nature of cluster formation, perhaps successive surface approaches alter and disrupt the clusters in different ways, despite the same approach velocity. However, we stress that in the above scaling analysis and most simulation and theory work, typically only monovalent ions are considered. MD simulations exploring the effect of valency will be vital to truly understand the interplay between ion cluster formation and anomalous underscreening.

Finally, we note that charge-inversion (and subsequent attraction) is frequently observed in dilute divalent electrolyte systems (75), wherein the surface charge of the interface switches polarity. While we do not measure the surface charge in our experiments, the surface forces measurements display very similar levels of attractive forces and adhesion across all salts investigated (*SI Appendix*, Figs. S12–S15), showing no evidence of charge inversion, even in the 0:3 electrolyte. A lack of charge inversion could be due to the altered solvation structure of the divalent cation in WiSEs. A lack of enhanced attractive forces in concentrated-divalent systems has also been recently observed in colloidal systems (85). An absence of charge inversion would be another manifestation of the radically altered interfacial structure and charge neutralization mechanism in these highly concentrated electrolytes with implications for attractive forces and aggregation phenomena in divalent salt solutions (85, 86).

Conclusions

How divalent ions and mixtures of ions order at charged interfaces in concentrated aqueous environments is a fundamental question with relevance to an incredibly diverse set of applications. In this work, we study concentrated aqueous LiTFSI and $Zn(TFSI)_2$, as well as mixtures of the two to probe both the short-range and long-range structure within the EDL.

We first explore the bulk structure of the electrolyte. WAXS data demonstrate that $TFSI^-$ exists in ordered structures, both as solvated anions as well as in anionic clusters. Increasing concentration of the divalent cation suppresses these clusters. While the arrangement of ions is affected by salt type, the actual solvation environment seems similar across our four studied electrolytes: Raman spectroscopy suggests that the $TFSI^-$ is within the solvation shell of the cation, irrespective of cation identity.

In contrast with the classical GCS framework, both the cation and anion play critical roles in the EDL in these multivalent concentrated environments, affecting both the short-range (layering)

and long-range (electrostatic decay length) structure. An example schematic is shown in *SI Appendix*, Fig. S16. We now summarize the structure, beginning with the mica surfaces and working outward. SFA measurements reveal that as the divalent cation concentration increases, the adlayer thickness doubles from ≈1.1 nm to 2.2 nm. Given these large thicknesses, the adlayer likely contains both anions and cations. This is consistent with previous work suggesting the solvation shells within the adlayer are unchanged from their bulk environments. The structure of this adlayer may also be dynamic, although further work is needed to confirm this.

Following the adlayer, all electrolytes display ordered layers. Notably, the size of these layers is insensitive to cation identity or valency but is similar to the solvated-anion spacing determined via WAXS measurements. This suggests that these layers are dictated by the size of the largest entity in solution. Changing the anion should accordingly change this layering structure.

All electrolytes exhibit underscreening, wherein their decay lengths are orders of magnitude larger than the classical Debye length. Additionally, the measured decay lengths from the SFA experiments are surprisingly insensitive to ion valency and display large run-to-run variability. In WiSEs, charge neutralization (the mechanistic origin of the decay length) is likely mediated by the formation of anionic clusters, rather than free ions. This helps explain the seemingly stochastic nature of the screening length, as well as its relative insensitivity to valency. Using independent measurements of cluster size and screening length, we compare our data with previously established theories and find that our scaling is consistent and that our fit line matches well with other mixed concentrated electrolyte systems.

These findings raise several critical implications. First, when thinking about reactivity, our results suggest that both the cation and anion are important in charge-transfer reactions where either ion is a reactant because of the impact each ion might have on the double-layer structure. This is a different picture than in a classical dilute electrolyte in which the counterion is the predominant species within the EDL and might be especially critical for multivalent systems (87). Additionally, the adlayers in these systems are quite thick, particularly for divalent electrolytes. For electrochemical applications, at the same applied potential as in a dilute electrolyte (with its associated smaller Stern layer), the potential drop within the adlayer (and corresponding electric field) will be quite different. This will alter the driving force (kinetics) for outer-sphere electron transfer reactions, and because of the different electric field, this may also alter how surface intermediates are stabilized for inner-sphere reactions. Additionally, this cluster mechanism undoubtedly impacts (and likely impedes) transport of product and reactant species.

Our work has revealed key insights into the structure of the EDL in concentrated multivalent environments. However, we stress that SFA measurements are not sensitive to chemical speciation, and additional work to resolve chemical identity partitioning within these EDLs is necessary. Additionally, most theory and simulation work has focused on monovalent ions. Continued exploration of divalent ions is sorely needed.

Materials and Methods

See *SI Appendix* for technical details for each method, including electrolyte preparation. **WAXS** was collected at the 11-BM CMS beamline of NSLS-II at a photon energy of 13.5 keV using quartz capillaries filled with electrolyte. An empty capillary was used to subtract out background signal from the electrolyte data. **Raman spectra** were recorded on a VERTEX 70 Fourier-transform infrared spectrometer with a RAM II FT-Raman Module (Bruker) equipped with a monochromatic laser source (1,064 nm) and a nitrogen-cooled Ge-diode detector in 5 mm NMR-tubes. All displayed spectra are normalized to the maximum intensity in the displayed range. **SFA measurements** were conducted in a SFA 2000 (SurForce LLC). Two mica-covered discs were mounted in a cross-cylinder geometry, with electrolyte injected between them. The bottom disc was mounted on a cantilever spring with a spring constant $K = (133 \pm 6)$ N/m, and driven via a microstepping motor (Faulhaber). The separation between our surfaces at any given point was analyzed via multiple-beam interferometry to generate the force-distance curves.

Data, Materials, and Software Availability. All study data are included in the article and/or *SI Appendix*.

Author affiliations: ^aDepartment of Chemical and Biomolecular Engineering, University of California, Berkeley, CA 94720; ^bMünster Electrochemical Energy Technology, University of Münster, Münster 48149, Germany; ^cPolymer Processing Group, Materials Science and Engineering Division, National Institute of Standards and Technology, Gaithersburg, MD 20899; ^dEnergy Storage and Distributed Resources Division, Lawrence Berkeley National Laboratory, Berkeley, CA 94720; and ^eHelmholtz-Institute Münster Ionics in Energy Storage, Münster 48149, Germany

Author contributions: S.A.B. and J.F. designed research; S.A.B., V.K., D.S., L.F., Z.D.L., B.D.M., M.W., and J.F. performed research; S.A.B., V.K., and P.J.D. analyzed data; and S.A.B., V.K., P.J.D., and J.F. wrote the paper.

1. L. Suo *et al.*, "Water-in-salt" electrolyte enables high-voltage aqueous lithium-ion chemistries. *Science* **350**, 938–943 (2015), 10.1126/science.aab1595.
2. O. Borodin *et al.*, Liquid structure with nano-heterogeneity promotes cationic transport in concentrated electrolytes. *ACS Nano* **11**, 10462–10471 (2017), 10.1021/acsnano.7b05664.
3. M. McEldrew, Z. A. H. Goodwin, S. Bi, A. A. Kornyshev, M. Z. Bazant, Ion clusters and networks in water-in-salt electrolytes. *J. Electrochem. Soc.* **168**, 050514 (2021), 10.1149/1945-7111/abf975.
4. J. Lim *et al.*, Nanometric water channels in water-in-salt lithium ion battery electrolyte. *J. Am. Chem. Soc.* **140**, 15661–15667 (2018), 10.1021/jacs.8b07696.
5. M. A. Gebbie, B. Liu, W. Guo, S. R. Anderson, S. G. Johnstone, Linking electric double layer formation to electrocatalytic activity. *ACS Catal.* **13**, 16222–16239 (2023), 10.1021/acscatal.3c04255.
6. L. Bellarosa, R. García-Muelas, G. Revilla-López, N. López, Diversity at the water-metal interface: Metal, water thickness, and confinement effects. *ACS Cent. Sci.* **2**, 109–116 (2016), 10.1021/acscentsci.5b00349.
7. J. N. Israelachvili, Ed., *Intermolecular and Surface Forces* (Academic Press, Boston, MA, ed. 3, 2011), p. iii, 10.1016/B978-0-12-391927-4.10024-6.
8. J. Wu, Understanding the electric double-layer structure, capacitance, and charging dynamics. *Chem. Rev.* **122**, 10821–10859 (2022), 10.1021/acs.chemrev.2c00097.
9. A. A. Lee, C. S. Perez-Martinez, A. M. Smith, S. Perkin, Scaling analysis of the screening length in concentrated electrolytes. *Phys. Rev. Lett.* **119**, 026002 (2017), 10.1103/PhysRevLett.119.026002.
10. M. A. Gebbie *et al.*, Long range electrostatic forces in ionic liquids. *Chem. Commun.* **53**, 1214–1224 (2017), 10.1039/C6CC08820A.
11. T. S. Groves, C. S. Perez-Martinez, R. Lhermerout, S. Perkin, Surface forces and structure in a water-in-salt electrolyte. *J. Phys. Chem. Lett.* **12**, 1702–1707 (2021), 10.1021/acs.jpclett.0c03718.
12. M. Han, R. Zhang, A. A. Gewirth, R. M. Espinosa-Marzal, Nanoheterogeneity of LiTFSI solutions transitions close to a surface and with concentration. *Nano Lett.* **21**, 2304–2309 (2021), 10.1021/acs.nanolett.1c00167.
13. P. Gaddam, W. Ducker, Electrostatic screening length in concentrated salt solutions. *Langmuir* **35**, 5719–5727 (2019), 10.1021/acs.langmuir.9b00375.
14. R. Zhang *et al.*, Potential-dependent layering in the electrochemical double layer of water-in-salt electrolytes. *ACS Appl. Energy Mater.* **3**, 8086–8094 (2020), 10.1021/acsaem.0c01534.
15. C.-Y. Li *et al.*, Unconventional interfacial water structure of highly concentrated aqueous electrolytes at negative electrode polarizations. *Nat. Commun.* **13**, 5330 (2022), 10.1038/s41467-022-33129-8.
16. L. Suo *et al.*, How solid-electrolyte interphase forms in aqueous electrolytes. *J. Am. Chem. Soc.* **139**, 18670–18680 (2017), 10.1021/jacs.7b10688.
17. N. Dubouis *et al.*, The role of the hydrogen evolution reaction in the solid-electrolyte interphase formation mechanism for "water-in-salt" electrolytes. *Energy Environ. Sci.* **11**, 3491–3499 (2018), 10.1039/C8EE02456A.
18. M. McEldrew, Z. A. H. Goodwin, A. A. Kornyshev, M. Z. Bazant, Theory of the double layer in water-in-salt electrolytes. *J. Phys. Chem. Lett.* **9**, 5840–5846 (2018), 10.1021/acs.jpclett.8b02543.
19. T. Ichii *et al.*, Solvation structure on water-in-salt/mica interfaces and its molality dependence investigated by atomic force microscopy. *Jpn. J. Appl. Phys.* **59**, SN1003 (2020), 10.35848/1347-4065/ab80a6.
20. T. Baimpos, B. R. Shrestha, S. Raman, M. Valtiner, Effect of interfacial ion structuring on range and magnitude of electric double layer, hydration, and adhesive interactions between mica surfaces in 0.05–3 M Li+ and Cs+ electrolyte solutions. *Langmuir* **30**, 4322–4332 (2014), 10.1021/la500288w.

21. R. M. Pashley, J. N. Israelachvili, DLVO and hydration forces between mica surfaces in Mg^{2+}, Ca^{2+}, Sr^{2+}, and Ba^{2+} chloride solutions *J. Colloid Interface Sci.* **97**, 446–455 (1984), 10.1016/0021-9797(84)90316-3.

22. S. S. Lee, A. Koishi, I. C. Bourg, P. Fenter, Ion correlations drive charge overscreening and heterogeneous nucleation at solid-aqueous electrolyte interfaces. *Proc. Natl. Acad. Sci. U.S.A.* **118**, e2105154118 (2021), 10.1073/pnas.2105154118.

23. J. Neumann, S. S. Lee, E. J. Zhao, P. Fenter, Direct experimental observations of ion distributions during overcharging at the muscovite-water interface by adsorption of Rb$^+$ and halides (Cl$^-$, Br$^-$, I$^-$) at high salinity *ChemPhysChem* 24, e202300545 (2023). 10.1002/cphc.202300545.

24. M. Han *et al.*, Insight into the electrical double layer of ionic liquids revealed through its temporal evolution. *Adv. Mater. Interfaces* **7**, 2001313 (2020), 10.1002/admi.202001313.

25. M. A. Gebbie *et al.*, Ionic liquids behave as dilute electrolyte solutions. *Proc. Natl. Acad. Sci. U.S.A.* **110**, 9674–9679 (2013), 10.1073/pnas.1307871110.

26. A. A. Lee, C. S. Perez-Martinez, A. M. Smith, S. Perkin, Underscreening in concentrated electrolytes. *Faraday Discuss.* **199**, 239–259 (2017), 10.1039/C6FD00250A.

27. M. Han, R. M. Espinosa-Marzal, Influence of water on structure, dynamics, and electrostatics of hydrophilic and hydrophobic ionic liquids in charged and hydrophilic confinement between mica surfaces. *ACS Appl. Mater. Interfaces* **11**, 33465–33477 (2019), 10.1021/acsami.9b10923.

28. N. Hjalmarsson, R. Atkin, M. W. Rutland, Switchable long-range double layer force observed in a protic ionic liquid. *Chem. Commun.* **53**, 647–650 (2017), 10.1039/C6CC07396D.

29. J. Nishida, J. P. Breen, B. Wu, M. D. Fayer, Extraordinary slowing of structural dynamics in thin films of a room temperature ionic liquid. *ACS Cent. Sci.* **4**, 1065–1073 (2018), 10.1021/acscentsci.8b00353.

30. M. Chu, M. Miller, P. Dutta, Crowding and anomalous capacitance at an electrode-ionic liquid interface observed using operando X-ray scattering. *ACS Cent. Sci.* **2**, 175–180 (2016), 10.1021/acscentsci.6b00014.

31. R. M. Espinosa-Marzal, Z. A. H. Goodwin, X. Zhang, Q. Zheng, Colloidal interactions in ionic liquids–The electrical double layer inferred from ion layering and aggregation. One hundred years of colloid symposia looking back and looking forward. ACS Symposium Series. *Am. Chem. Soc.* **1457**, 123–148 (2023). 10.1021/bk-2023-1457.ch007.

32. A. Härtel, M. Bültmann, F. Coupette, Anomalous underscreening in the restricted primitive model. *Phys. Rev. Lett.* **130**, 108202 (2023), 10.1103/PhysRevLett.130.108202.

33. F. Coupette, A. A. Lee, A. Härtel, Screening lengths in ionic fluids. *Phys. Rev. Lett.* **121**, 075501 (2018), 10.1103/PhysRevLett.121.075501.

34. Z. A. H. Goodwin, A. A. Kornyshev, Underscreening, overscreening and double-layer capacitance. *Electrochem. Commun.* **82**, 129–133 (2017), 10.1016/j.elecom.2017.07.008.

35. A. A. Lee, D. Vella, S. Perkin, A. Goriely, Are room-temperature ionic liquids dilute electrolytes? *J. Phys. Chem. Lett.* **6**, 159–163 (2015), 10.1021/jz502250z.

36. S. Perkin, M. Salanne, P. Madden, R. Lynden-Bell, Is a stern and diffuse layer model appropriate to ionic liquids at surfaces? *Proc. Natl. Acad. Sci. U.S.A.* **110**, E4121 (2013), 10.1073/pnas.1314188110.

37. M. A. Gebbie *et al.*, Experimental observations demonstrate that ionic liquids form both bound (Stern) and diffuse electric double layers. *Proc. Natl. Acad. Sci. U.S.A.* **110**, E4122 (2013), 10.1073/pnas.1315608110.

38. R. Kjellander, A multiple decay-length extension of the Debye–Hückel theory: To achieve high accuracy also for concentrated solutions and explain under-screening in dilute symmetric electrolytes. *Phys. Chem. Chem. Phys.* **22**, 23952–23985 (2020), 10.1039/D0CP02742A.

39. R. Kjellander, Focus article: Oscillatory and long-range monotonic exponential decays of electrostatic interactions in ionic liquids and other electrolytes: The significance of dielectric permittivity and renormalized charges. *J. Chem. Phys.* **148**, 193701 (2018), 10.1063/1.5010024.

40. R. Kjellander, Nonlocal electrostatics in ionic liquids: The key to an understanding of the screening decay length and screened interactions. *J. Chem. Phys.* **145**, 124503 (2016), 10.1063/1.4962756.

41. B. Rotenberg, O. Bernard, J.-P. Hansen, Underscreening in ionic liquids: A first principles analysis. *J. Phys. Condens. Matter* **30**, 054005 (2018), 10.1088/1361-648X/aaa3ac.

42. E. Krucker-Velasquez, J. W. Swan, Underscreening and hidden ion structures in large scale simulations of concentrated electrolytes. *J. Chem. Phys.* **155**, 134903 (2021), 10.1063/5.0061230.

43. P. Cats, R. Evans, A. Härtel, R. van Roij, Primitive model electrolytes in the near and far field: Decay lengths from DFT and simulations. *J. Chem. Phys.* **154**, 124504 (2021), 10.1063/5.0039619.

44. J. Zeman, S. Kondrat, C. Holm, Bulk ionic screening lengths from extremely large-scale molecular dynamics simulations. *Chem. Commun.* **56**, 15635–15638 (2020), 10.1039/D0CC05023G.

45. R. M. Adar, S. A. Safran, H. Diamant, D. Andelman, Screening length for finite-size ions in concentrated electrolytes. *Phys. Rev. E* **100**, 042615 (2019), 10.1103/PhysRevE.100.042615.

46. R. P. Misra, J. P. De Souza, D. Blankschtein, M. Z. Bazant, Theory of surface forces in multivalent electrolytes. *Langmuir* **35**, 11550–11565 (2019), 10.1021/acs.langmuir.9b01110.

47. F. Wang *et al.*, Highly reversible zinc metal anode for aqueous batteries. *Nat. Mater.* **17**, 543–549 (2018), 10.1038/s41563-018-0063-z.

48. K. V. Kravchyk, M. V. Kovalenko, Aluminum electrolytes for Al dual-ion batteries. *Commun. Chem.* **3**, 1–9 (2020), 10.1038/s42004-020-00365-2.

49. W. Giurlani *et al.*, Specific ion effects on copper electroplating. *Colloids Surf. B, Biointerfaces* **225**, 113287 (2023), 10.1016/j.colsurfb.2023.113287.

50. J. Rubio-Garcia, J. Cui, A. Parra-Puerto, A. Kucernak, Hydrogen/vanadium hybrid redox flow battery with enhanced electrolyte concentration. *Energy Storage Mater.* **31**, 1–10 (2020), 10.1016/j.ensm.2020.05.031.

51. P. Meister *et al.*, Enabling Mg-based ionic liquid electrolytes for hybrid dual-ion capacitors. *Batteries Supercaps* **4**, 504–512 (2021), 10.1002/batt.202000246.

52. Z. Xiong *et al.*, A high-performance dual-ion battery-supercapacitor hybrid device based on LiCl in ion liquid dual-salt electrolyte. *Adv. Energy Mater.* **12**, 2103226 (2022), 10.1002/aenm.202103226.

53. V. A. Bloomfield, Condensation of DNA by multivalent cations: Considerations on mechanism. *Biopolymers* **31**, 1471–1481 (1991), 10.1002/bip.360311305.

54. M. A. Schumacher, A. F. Rivard, H. P. Bächinger, J. P. Adelman, Structure of the gating domain of a Ca^{2+}-activated K$^+$ channel complexed with Ca^{2+}/calmodulin. *Nature* **410**, 1120–1124 (2001), 10.1038/35074145.

55. J. W. Torrance, M. W. MacArthur, J. M. Thornton, Evolution of binding sites for zinc and calcium ions playing structural roles. *Proteins Struct. Funct. Bioinf.* **71**, 813–830 (2008), 10.1002/prot.21741.

56. O. Matsarskaia, F. Roosen-Runge, F. Schreiber, Multivalent ions and biomolecules: Attempting a comprehensive perspective. *ChemPhysChem* **21**, 1742–1767 (2020), 10.1002/cphc.202000162.

57. B. Seantier, B. Kasemo, Influence of mono- and divalent ions on the formation of supported phospholipid bilayers via vesicle adsorption. *Langmuir* **25**, 5767–5772 (2009), 10.1021/la804172f.

58. Y. Zhang *et al.*, Water or anion? Uncovering the Zn^{2+} solvation environment in mixed Zn(TFSI)$_2$ and LiTFSI water-in-salt electrolytes. *ACS Energy Lett.* **6**, 3458–3463 (2021), 10.1021/acsenergylett.1c01624.

59. X. Liu *et al.*, Microscopic understanding of the ionic networks of "water-in-salt" electrolytes. *Energy Mater. Adv.* **2021**, 7368420 (2021), 10.34133/2021/7368420.

60. M. S. Ding, L. Ma, M. A. Schroeder, K. Xu, Phase diagram and conductivity of Zn(TFSI)$_2$–H$_2$O electrolytes. *J. Phys. Chem. C* **124**, 25249–25253 (2020), 10.1021/acs.jpcc.0c07937.

61. W. J. R. Gilbert *et al.*, Density, viscosity, and vapor pressure measurements of water + lithium bis(trifluoromethylsulfonyl)imide solutions. *J. Chem. Eng. Data* **62**, 2056–2066 (2017), 10.1021/acs.jced.7b00135.

62. X. Liu *et al.*, Insight into the nanostructure of "water in salt" solutions: A SAXS/WAXS study on imide-based lithium salts aqueous solutions. *Energy Storage Mater.* **45**, 696–703 (2022), 10.1016/j.ensm.2021.12.016.

63. K. Qian, R. E. Winans, T. Li, Insights into the nanostructure, solvation, and dynamics of liquid electrolytes through small-angle X-ray scattering. *Adv. Energy Mater.* **11**, 2002821 (2021), 10.1002/aenm.202002821.

64. Y. Zhang *et al.*, Water-in-salt LiTFSI aqueous electrolytes. 1. Liquid structure from combined molecular dynamics simulation and experimental studies. *J. Phys. Chem. B* **125**, 4501–4513 (2021), 10.1021/acs.jpcb.1c02189.

65. X. Liu *et al.*, Revealing the correlation between the solvation structures and the transport properties of water-in-salt electrolytes. *Chem. Mater.* **35**, 2088–2094 (2023), 10.1021/acs.chemmater.2c03654.

66. V. Küpers *et al.*, Opportunities and limitations of ionic liquid- and organic carbonate solvent-based electrolytes for Mg-ion-based dual-ion batteries. *ChemSusChem* **14**, 4480–4498 (2021), 10.1002/cssc.202101227.

67. A. V. Cresce *et al.*, Solvation behavior of carbonate-based electrolytes in sodium ion batteries. *Phys. Chem. Chem. Phys.* **19**, 574–586 (2017), 10.1039/C6CP07215A.

68. C. D. van Engers, Z. D. Lamberty, P. M. McGuiggan, J. Frechette, Template-stripped ultra-smooth aluminum films (0.2 Nm RMS) for the surface forces apparatus. *Langmuir* **37**, 6556–6565 (2021), 10.1021/acs.langmuir.1c00899.

69. J. Israelachvili *et al.*, Recent advances in the surface forces apparatus (SFA) technique. *Rep. Prog. Phys.* **73**, 036601 (2010), 10.1088/0034-4885/73/3/036601.

70. J. S. Lyons, D. N. Furlong, T. W. Healy, The electrical double-layer properties of the mica (muscovite)-aqueous electrolyte interface. *Aust. J. Chem.* **34**, 1177–1187 (1981), 10.1071/ch9811177.

71. V. E. Shubin, P. Kékicheff, Electrical double layer structure revisited via a surface force apparatus: Mica interfaces in lithium nitrate solutions. *J. Colloid Interface Sci.* **155**, 108–123 (1993), 10.1006/jcis.1993.1016.

72. R. M. Pashley, Hydration forces between mica surfaces in aqueous electrolyte solutions. *J. Colloid Interface Sci.* **80**, 153–162 (1981), 10.1016/0021-9797(81)90171-5.

73. P. J. Sides, D. Faruqui, A. J. Gellman, Dynamics of charging of muscovite mica: Measurement and modeling. *Langmuir* **25**, 1475–1481 (2009), 10.1021/la802752g.

74. A. R. Crothers, C. Li, C. J. Radke, A grahame triple-layer model unifies mica monovalent ion exchange, zeta potential, and surface forces. *Adv. Colloid Interface Sci.* **288**, 102335 (2021), 10.1016/j.cis.2020.102335.

75. P. Kékicheff, S. Marcelja, T. J. Senden, V. E. Shubin, Charge reversal seen in electrical double layer interaction of surfaces immersed in 2:1 calcium electrolyte. *J. Chem. Phys.* **99**, 6098–6113 (1993). 10.1063/1.465906.

76. R. M. Espinosa-Marzal, T. Drobek, T. Balmer, M. P. Heuberger, Hydrated-Ion Ordering in Electrical Double Layers. *Phys. Chem. Chem. Phys.* **14**, 6085–6093 (2012), 10.1039/C2CP40255F.

77. Z. Zachariah, M. P. Heuberger, R. M. Espinosa-Marzal, Colloidal interactions–DLVO theory and beyond. One hundred years of colloid symposia looking back and looking forward. ACS Symposium Series. *Am. Chem. Soc.* **1457**, 31–47 (2023). 10.1021/bk-2023-1457.ch002.

78. S. J. T. Brugman *et al.*, Monovalent-divalent cation competition at the muscovite mica surface: Experiment and theory. *J. Colloid Interface Sci.* **559**, 291–303 (2020), 10.1016/j.jcis.2019.10.009.

79. V. Gómez-González *et al.*, Molecular dynamics simulation of the structure and interfacial free energy barriers of mixtures of ionic liquids and divalent salts near a graphene wall. *Phys. Chem. Chem. Phys.* **19**, 846–853 (2016), 10.1039/C6CP07002G.

80. G. Horwitz *et al.*, The nanostructure of water-in-salt electrolytes revisited: Effect of the anion size. *ACS Nano* **15**, 11564–11572 (2021), 10.1021/acsnano.1c01737.

81. S. A. Safran, A. Pincus, Scaling perspectives of underscreening in concentrated electrolyte solutions. *Soft Matter* **19**, 7907–7911 (2023), 10.1039/D3SM01094E.

82. Z. A. H. Goodwin, A. A. Kornyshev, Cracking ion pairs in the electrical double layer of ionic liquids. *Electrochim. Acta* **434**, 141163 (2022), 10.1016/j.electacta.2022.141163.

83. Z. A. H. Goodwin, M. McEldrew, J. Pedro de Souza, M. Z. Bazant, A. A. Kornyshev, Gelation, clustering, and crowding in the electrical double layer of ionic liquids. *J. Chem. Phys.* **157**, 094106 (2022), 10.1063/5.0097055.

84. M. Prencipe, A. Zupan, R. Dovesi, E. Aprà, V. R. Saunders, Ab Initio study of the structural properties of LiF, NaF, KF, LiCl, NaCl, and KCl. *Phys. Rev. B* **51**, 3391–3396 (1995), 10.1103/PhysRevB.51.3391.

85. R. J. E. Reinertsen *et al.*, Reexpansion of charged nanoparticle assemblies in concentrated electrolytes. *Proc. Natl. Acad. Sci. U.S.A.* **121**, e2316537121 (2024), 10.1073/pnas.2316537121.

86. D. Pastré *et al.*, Adsorption of DNA to mica mediated by divalent counterions: A theoretical and experimental study. *Biophys. J.* **85**, 2507–2518 (2003), 10.1016/S0006-3495(03)74673-6.

87. N. N. Rajput, X. Qu, N. Sa, A. K. Burrell, K. A. Persson, The coupling between stability and ion pair formation in magnesium electrolytes from first-principles quantum mechanics and classical molecular dynamics. *J. Am. Chem. Soc.* **137**, 3411–3420 (2015), 10.1021/jacs.5b01004.